Angewandte Chemie
Eine Zeitschrift der Gesellschaft Deutscher Chemiker

Supporting Information

Theoretical Optimization of Compositions of High-Entropy Oxides for the Oxygen Evolution Reaction

K. L. Svane, J. Rossmeisl*

S1. COMPUTATIONAL METHODS

A. DFT setup

Density functional theory calculations are performed using the gridbased projector augmented wave (GPAW) software package with the atomic simulation environment (ASE) used to set up and analyse the calculations.[1–3] A plane-wave basis set with an energy cutoff of 500 eV is used, and the exchange and correlation energy is calculated with the RPBE functional.[4] The surface is modelled as a 3×1 slab of the rutile (110) surface and the brilouin zone is sampled by 2×2 k-points. The slab has four layers of atoms, of which the bottom two layers are fixed to the bulk positions. 10 Å of vacuum is added on either sides of the slab and a dipole correction is used to decouple the electrostatic potentials. The structures are relaxed until the forces on all atoms are below $0.05\,\mathrm{eV\,Å^{-1}}$.

B. Choice of lattice constant

The experimental and computationally optimised lattice constants of the five pure metal oxides are given in Table S1. The lattice constants of the high entropy oxide is set to the

TABLE S1. Lattice constants of rutile oxides. Experimental data is taken from Ref. 5.

	Ru	Ti	Ir	Rh	Os
a DFT	4.57	4.70	4.59	4.60	4.56
a Exp.	4.49	4.59	4.50	4.49	4.50
c DFT	3.14	2.99	3.19	3.14	3.19
c Exp.	3.11	2.96	3.15	3.09	3.18
a/c DFT	1.46	1.57	1.44	1.47	1.43

optimised lattice constants for RuO_2 which are within 2% and 5% of the a and c lattice constants of the five pure rutile oxides, respectively. Figure S1 shows that the choice of lattice constant within this range has a very small effect on the calculated overpotential, except in the case of TiO_2, which has a somewhat different a/c ratio than the other oxides.

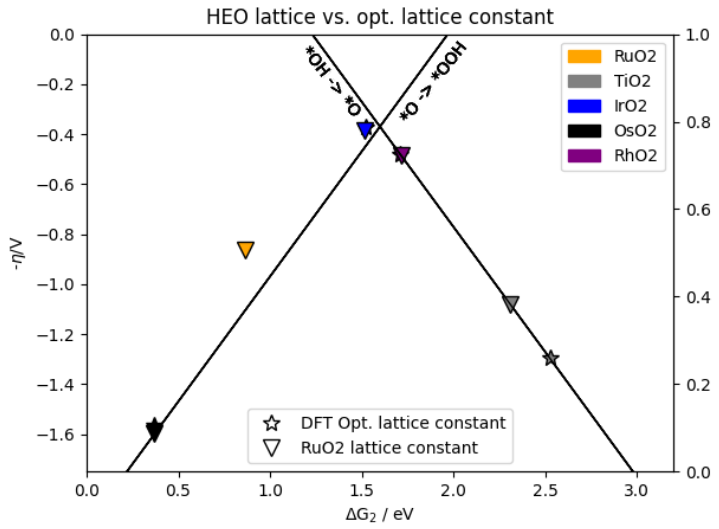

FIG. S1. Calculated overpotential vs. ΔG_2 for the five rutile metal oxides. The overpotential is calculated for the conventional pathway on a surface with 2/3 *O coverage for the metals on the strong binding side of the volcano (Os, Ru, Ir), and on a bare surface for the metals on the weak binding side of the volcano (Ti, Rh).

C. Adsorption energy calculations

The adsorption energy of an adsorbate (A = O,OH) is calculated as:

$$\Delta E_{ads}(A) = E_{slab+A} + \tfrac{n}{2}E_{H_2} - E_{slab} - E_{H_2O} \tag{1}$$

where E_{slab+A} is the energy of the slab with the adsorbate, E_{slab} is the energy of the slab without the adsorbate, E_{H_2}, E_{H_2O} are the energies of H_2 and H_2O in the gas phase, respectively, and n is the number of electrons involved in the reaction. The adsorption energies are calculated for a surface with 2/3 coverage of oxygen on the cus sites, i.e. the reaction is proceeding on the only vacant cus site in the unit cell. This coverage is a reasonable representation of the surface close to the onset potential, since the conversion of *O to *OOH is the limiting step in the reaction on most sites. The coverage dependence of the adsorption energies of *OH and *O (obtained with the fitted model described in Section S5 below) is shown in Figure S2, demonstrating that the distributions shift towards weaker binding for increasing coverages of pre-adsorbed *O.

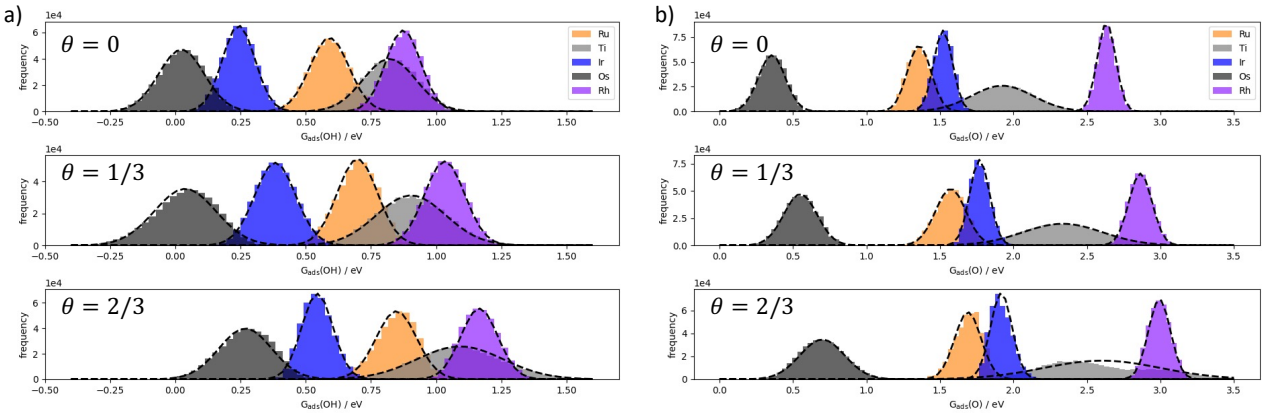

FIG. S2. Distribution of adsorption energies on the cus site for a) *OH and b) *O obtained with fitted models at different coverages (θ) of pre-adsorbed *O.

The adsorption energy calculated by DFT does not include the effects of potential, zero point energy, entropy and solvation. The effect of an applied potential is described using the computational hydrogen electrode,[6] while estimates of the free energy corrections of 0.35, 0.05 and 0.40 eV taken from ref. 7 are used for *OH, *O and *OOH, respectively.

D. Further comments on the choice of functional and free energy correction

For ORR on metals it is experimentally established that Pt is positioned ca. 0.1 eV from the top of the volcano and free energy corrections can thus be chosen such that theoretical calculations are aligned with this result.[8] For OER the exact position of the pure oxides on the activity volcano are not known, but three qualitative observations haven been determined experimentally: (i) Both IrO_2 and RuO_2 are on the strongly bound side of the volcano, (ii) RuO_2 binds *O and *OH stronger than IrO_2 and (iii) RuO_2 is slightly more active than IrO_2.[9–11] With the chosen free energy corrections observations (i) and (ii) are reproduced, while observation (iii) can not be reproduced by modifying the corrections without contradicting observation (i). The incorrect ordering of the activities of RuO_2 and IrO_2 may be a result of the computational setup as well as the assumed reaction pathway.[12,13]

Figure S3 shows the calculated overpotential for pure RuO_2 and IrO_2 with the RPBE and BEEF-vdW[14] functionals, considering the conventional pathway and the bridge pathway at low and high coverage. The pathway with the lowest energy structure for each intermediate

is also indicated, for both functionals this is the bridge pathway for RuO_2 while for IrO_2 the reaction goes through the *OH and the $*O_2$ + H_b intermediates. Our calculations find that IrO_2 is more active than RuO_2, in contradiction with experimental results. This is a common result across several DFT functionals and implementations, but the correct ordering for the conventional pathway can be reproduced with explicit solvation and van der Waals corrections.[12] Figure S3b shows that the correct ordering is also found with the BEEF-vdW functional if the bridge pathway is considered. This functional furthermore allows us to estimate the uncertainty in the relative positions of the points for RuO_2 and IrO_2 by calculating the energies with an ensemble of 2000 different exchange-correlation functionals. The ellipses in Figure S3b represent one standard deviation and are calculated by first calculating the ensemble of adsorption energies following Eqn 1 in the main paper and then referencing the value to Ir, e.g. for the x-axis we calculate:

$$\Delta E_x = \Delta(\Delta G_2) = \Delta E_{ads,Ru}(O) - \Delta E_{ads,Ru}(OH) - (\Delta E_{ads,Ir}(O) - \Delta E_{ads,Ir}(OH))$$

and correspondingly, if ΔG_3 is the rate limiting step that determines the position on the y-axis:

$$\Delta E_y = \Delta(\Delta G_3) = \Delta E_{ads,Ru}(OOH) - \Delta E_{ads,Ru}(O) - (\Delta E_{ads,Ir}(OOH) - \Delta E_{ads,Ir}(O))$$

The ellipses are created following the procedure described in ref. 15. First, the covariance matrix is calculated:

$$cov(\Delta E_x, \Delta E_y) = \begin{bmatrix} \sigma_x^2 & \sigma_x\sigma_y \\ \sigma_x\sigma_y & \sigma_y^2 \end{bmatrix}$$

where σ_x and σ_y are the standard deviations of the data in ΔE_x and ΔE_y, respectively. The Pearson coefficient is then calculated as:

$$p = \frac{cov(\Delta E_x, \Delta E_y)}{\sigma_x\sigma_y}$$

From the Pearson coefficient an ellipse can be drawn with horizontal and vertical radius (r_h and r_v, respectively):

$$r_h = \sqrt{1+p}$$
$$r_v = \sqrt{1-p}$$

The ellipse is rotated counterclockwise around its center by 45° and scaled by $2n\sigma_x$ and $2n\sigma_y$ in the x- and y-direction, respectively, to obtain an ellipse that represents n standard deviations. The position of the center of the ellipse is calculated by averaging the values representing the x- and y-axis across the 2000 functionals in the ensemble. The ellipses show that the one standard deviation is on the order of 0.1 eV and roughly follows the left leg of the volcano. Clearly the results are sensitive to the choice of functional, and the magnitude of the uncertainty is large enough that it may explain the incorrect ordering of the activities calculated with RPBE.

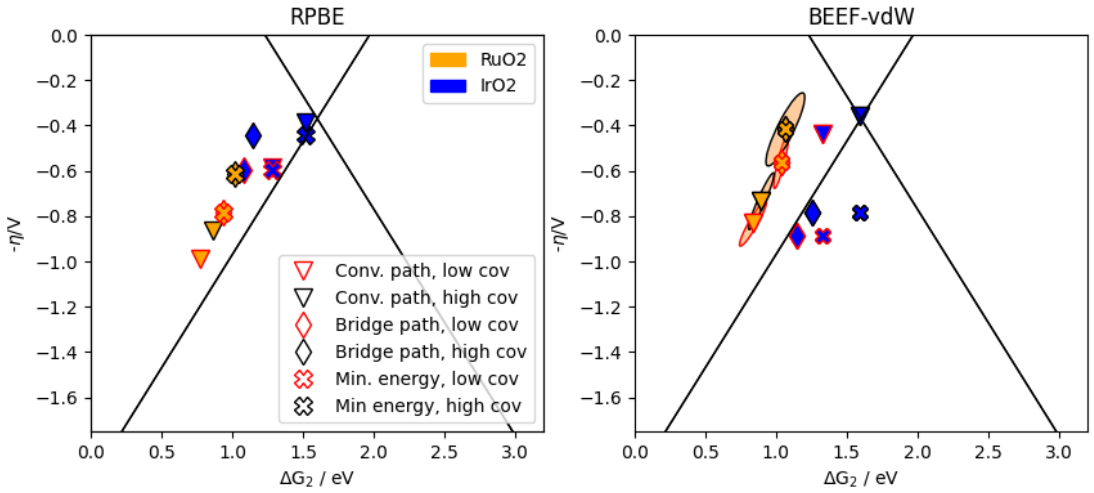

FIG. S3. Calculated overpotential vs. ΔG_2 for IrO_2 and RuO_2 at low and high coverage and following different pathways with a) the RPBE functional and b) the BEEF-vdW functional. Ellipses calculated with the BEEF-vdW functional represent one standard deviation of the relative positions of IrO_2 and RuO_2 points as calculated with the ensemble of functionals.

An alternative explanation for the incorrect ordering of the RuO_2 and IrO_2 activities could be that the correct reaction intermediates have not been considered. At high coverage on IrO_2 we find that it is favourable for *OOH to transfer a proton to a negihbouring *O, resulting in a calculated overpotential below that of RuO_2. This pathway however relies on the presence of adsorbed *O on the neighbouring site, therefore it will not be possible to follow for all sites simultaneously. This possibility has therefore not been included in our explicit model of the HEO surface.

S2. ENTHALPY OF MIXING

Figure S4 shows the enthalpy of mixing 1/12 of one oxide in the bulk of each of the other oxides. The lattice constant is kept at the lattice constant of the host oxide as given in Table S1. The plot shows that all elements except for Ti are readily mixed. This result may arise from the different lattice parameters and a/c ratio for TiO_2 compared with the other oxides. Since the entropy contribution to the free energy of mixing is negative, it might still be possible to form HEOs with Ti.

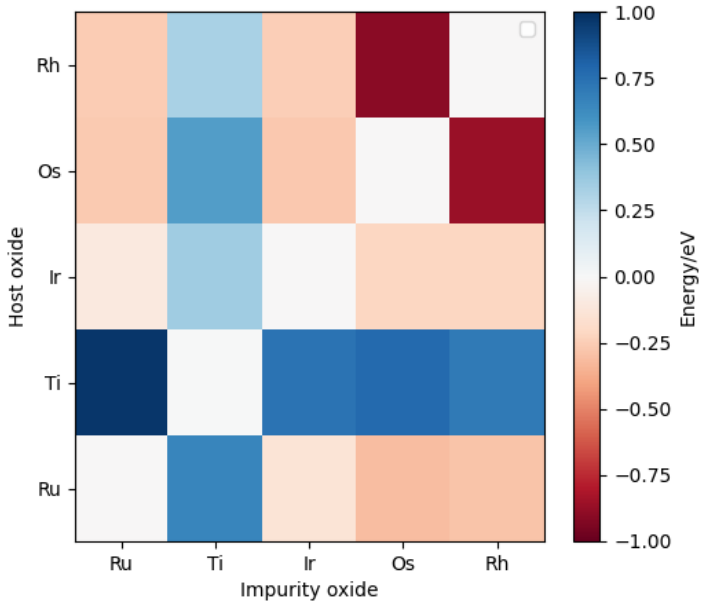

FIG. S4. Enthalpy of replacing 1/12 of the metal atoms in a rutile oxide with another metal.

S3. DISTRIBUTION OF O ADSORPTION ENERGIES

Figure S5 shows a histogram of the DFT calculated *O adsorption energies and the corresponding histogram for all possible sites obtained with the fitted model.

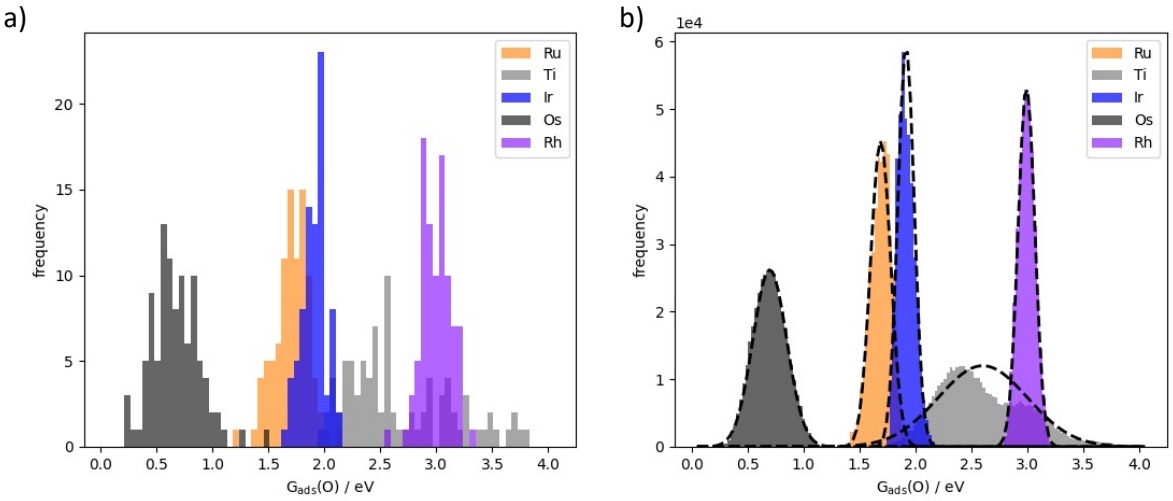

FIG. S5. Distribution of adsorption energies on the cus site for *O a) as calculated by DFT for 450 adsorption sites and b) obtained with the fitted model. The results are for a surface with 2/3 of all cus sites already covered by *O.

S4. SCALING RELATIONS FOLLOWING THE BRIDGE PATHWAY

Figure S6a and b show the scaling relations between the adsorption energies of *OH/*OOH and *O + H_b/*O_2 + H_b, respectively. Fitting all points to a line with a slope of 1 for the conventional pathway gives the result $G_{ads}(OOH) = G_{ads}(OH) + 3.2\,\text{eV}$ well known from normal oxide surfaces.[16] For the bridge pathway a fit for each element on the *O/*O_2 adsorption site is made, with fitted energy differences given in Table S2. The different scaling relations arise because the binding of anionic *O and molecular *O_2 are not interdependent in the same way as *OH and *OOH. If *O_2 has a binding energy of 0 eV the scaling relation between *O + H_b and *O_2 + H_b should be equal to 4.92 eV - $G_{ads}(O)$. Table S2 show that this is approximately true, with the largest deviations for Ti and Os. The deviations indicate a significant positive or negative binding energy of O_2 on Ti and Os, respectively.

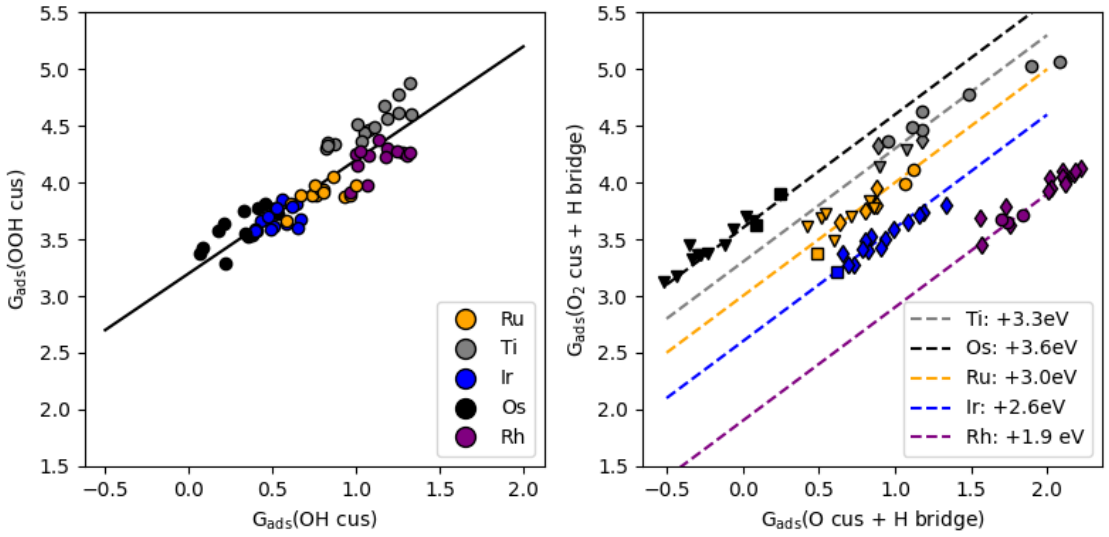

FIG. S6. Scaling relations a) between the adsorption energy of *OH and *OOH and b) between the adsorption energies of *O + H_b and *O_2 + H_b. Circles and triangles indicate sites that follow the conventional and bridge pathway, respectively, while squares represent sites where the *O + H_b and *OOH intermediates are preferred and diamonds represent sites where the *OH and *O_2+ H_b intermediates are preferred. Lines indicate the best linear fit with a slope of 1.

It should be noted that O_2(g) in the ground (triplet) state is poorly described by DFT, and calculations with O_2(g) as reference are avoided by using H_2O as reference. Some of this error may however still be present in adsorbed O_2, giving some uncertainty to the exact value

TABLE S2. Scaling relation following the bridge pathway from fit to DFT calculated values and assuming that O_2 has a binding energy of 0 eV. All values are in eV.

	$G_{ads}(O)$ av., high cov.	Scaling (from fit)	Scaling (from $G_{ads}(O)$)
Ru	1.69	3.0	3.23
Ti	2.60[a]	3.3	2.32
Ir	1.92	2.6	3.00
Os	0.70	3.6	4.22
Rh	2.99	1.9	1.93

[a] The distribution of *O binding energies at high coverage has two peaks and might not be well described by this average value (c.f. Figure S5).

for the scaling constants. With H_2O used as reference the calculated adsorption energies are lower bounds for the actual values.

S5. DETAILS OF LINEAR FIT

A. Excluding structures

The adsorption energies on the pure oxide structures are not included in the fit, as the electronic structure may be significantly different in the pure oxide and the HEO, and therefore difficult to describe in the same fit. This is clearly the case for TiO_2, which is a semiconductor in its pure form, while the HEO is conducting.

Upon optimisation some structures change from the intended original structure, which may also have unintended effects on the subsequent fitting. In particular, we observed the two following types of optimisation problems:

1) When two Rh atoms with *O adsorbed are next to each other, the oxygen atoms may combine to form $*O_2$. Such structures are re-optimised with the O-atoms constrained to move along the z-direction only.

2) A hydrogen from the bridge site may jump back to *O or $*O_2$ on the cus site, or vice versa. Such structures are given a weight of 0 in the fits, and are not included in the plots in the main paper either.

B. Linear model and included coefficients

The DFT calculated energies are used to make a linear fit, where the adsorption energy on site i (E^i_{ads}), depends on the number of atoms of each element (k) that are present in each of the three types of NN sites ($N^i_{cus,k}, N^i_{b,k}, N^i_{sub,k}$), but not on their relative locations:

$$E^i_{ads} = C_0 + \sum_k^{metals} C_{cus,k} N^i_{cus,k} + \sum_k^{metals} C_{b,k} N^i_{b,k} + \sum_k^{metals} C_{sub,k} N^i_{sub,k} \quad (2)$$

Five independent fits are made according to the identity of atom i. For the bridge site, two metal atoms form the adsorption site, resulting in a total of 15 combinations that are fitted independently. The expression for E^i_{ads} is of a similar form, but with additional coefficients to reflect that the bridge site has five different types of NN sites as shown in Figure 4a of the main paper. Including the NN sites only, there are $5^9 = 1.95 \cdot 10^6$ different cus sites, and

$5^{13} = 1.22 \cdot 10^9$ different bridge site. Some of these sites will however be equivalent due to rotational and mirror symmetry and the actual number of non-equivalent structures might therefore be lower by a factor $f < 4$. We note that there are only 78750 different cus sites and $17.7 \cdot 10^6$ different bridge sites within our model, since it does not include the relative positions of the NN atoms. These sites have been weighted by their relative probability in the various plotted distributions.

To test the stability of the linear fit, 100 fits are performed, with the data split in a training set (80%) and a test set (20%). The average fitting coefficients are plotted in Figure S7 for *OH and *O (with 2/3 *O coverage) with error bars indicating the standard deviation of their value. The coefficients are numbered along the x-axis such that coefficient 0-4 relate to the NN cus site ($C_{cus,k}$), coefficient 5-9 relate to the NN bridge site ($C_{b,k}$) and coefficient 10-14 relate to the subsurface sites ($C_{sub,k}$).

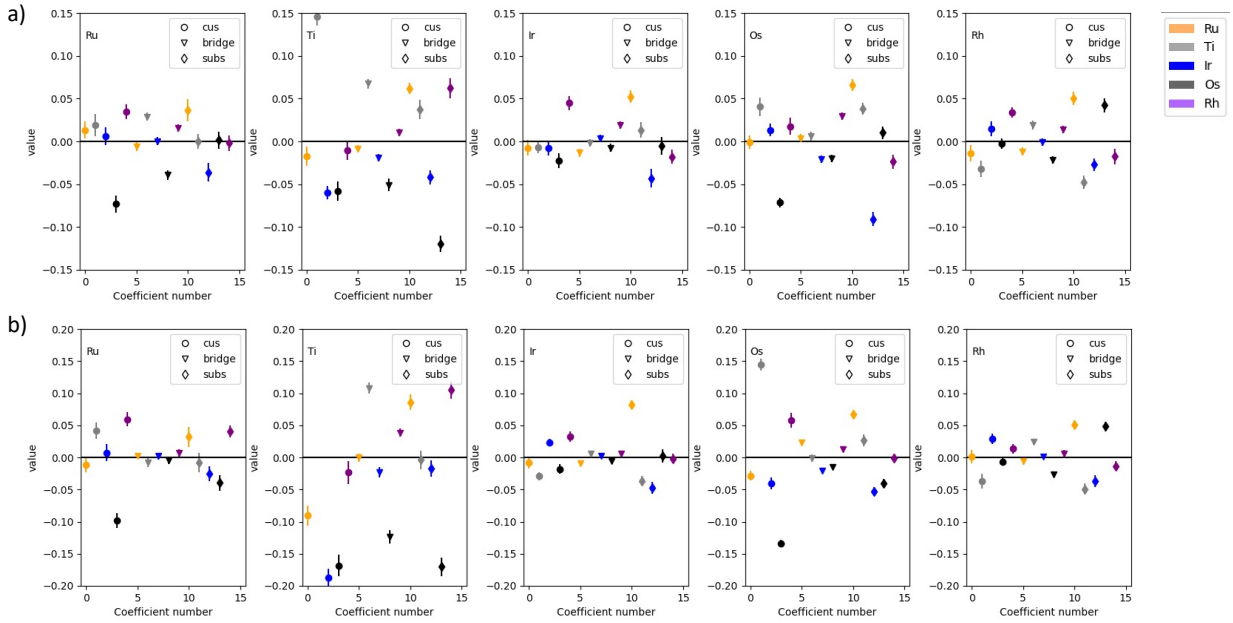

FIG. S7. Average fitting coefficients and standard deviation for 100 fits for a) *OH and b) *O at the cus site on a surface with 2/3 coverage of *O. The five plots refer to each of the five metals as adsorption sites as written in the top left corner. The colour of each marker indicate the identity of the atom (k) in the NN position.

C. Additional coefficients in the fit

The fit used for the main article assumes that only NN metal atoms have a significant effect on the adsorption energies. To test this assumption, the inclusion of additional atoms in the fit was attempted. Note, that with the chosen size of the unit cell not all next nearest neighbour (NNN) atoms can be included as some of them are identical to NN atoms or to the adsorption site itself. Therefore, only atoms that are not already part of the fit are included, as indicated in Figure S8.

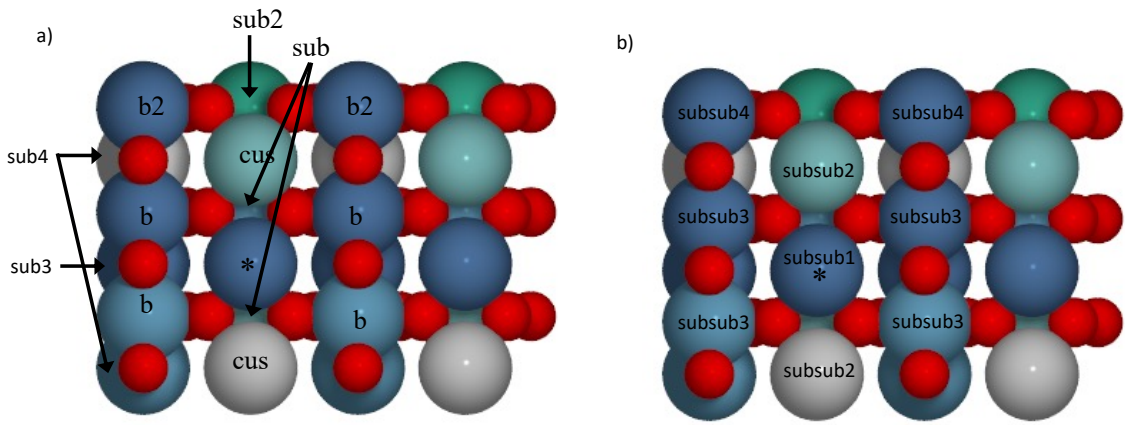

FIG. S8. Sites included in the extended fit a) in the surface and sub-surface layer and b) in the sub-subsurface layer. Atoms in the sub-subsurface layer can not be visualised, but are located directly below the marked sites in the top layer in b).

The resulting fitting coefficients are shown in Figure S9, S10 and S11. Most of the new coefficients are significantly smaller than the coefficients relating to the NN atoms, with the largest values found for the sub2 and subsub1 positions located in the rows of atoms directly below the adsorption site. Furthermore, the original NN coefficients are largely the same when additional atoms are included in the fit. Altogether, this justifies the choice of including NN atoms only in the fit.

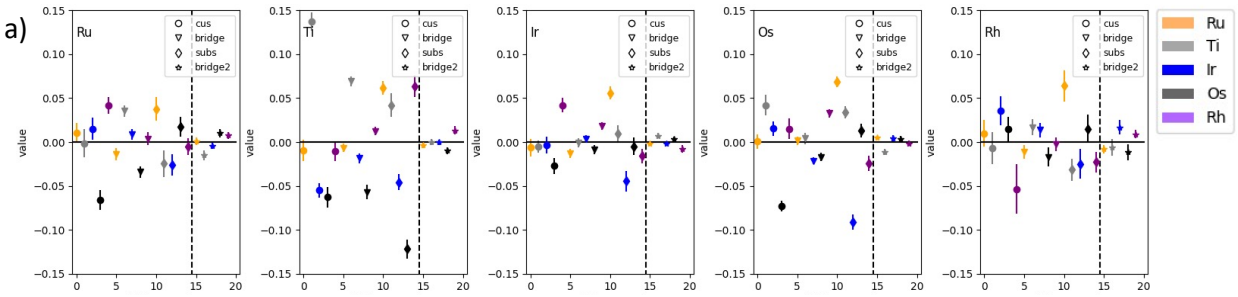

FIG. S9. Fitting coefficients for the adsorption of OH when including atoms marked b2 in the surface layer. The five plots refer to each of the five metals as adsorption sites as written in the top corner. The colour of each marker indicate the identity of the atom in the NN position. Markers to the right of the dashed line are the new coefficients included in the fit.

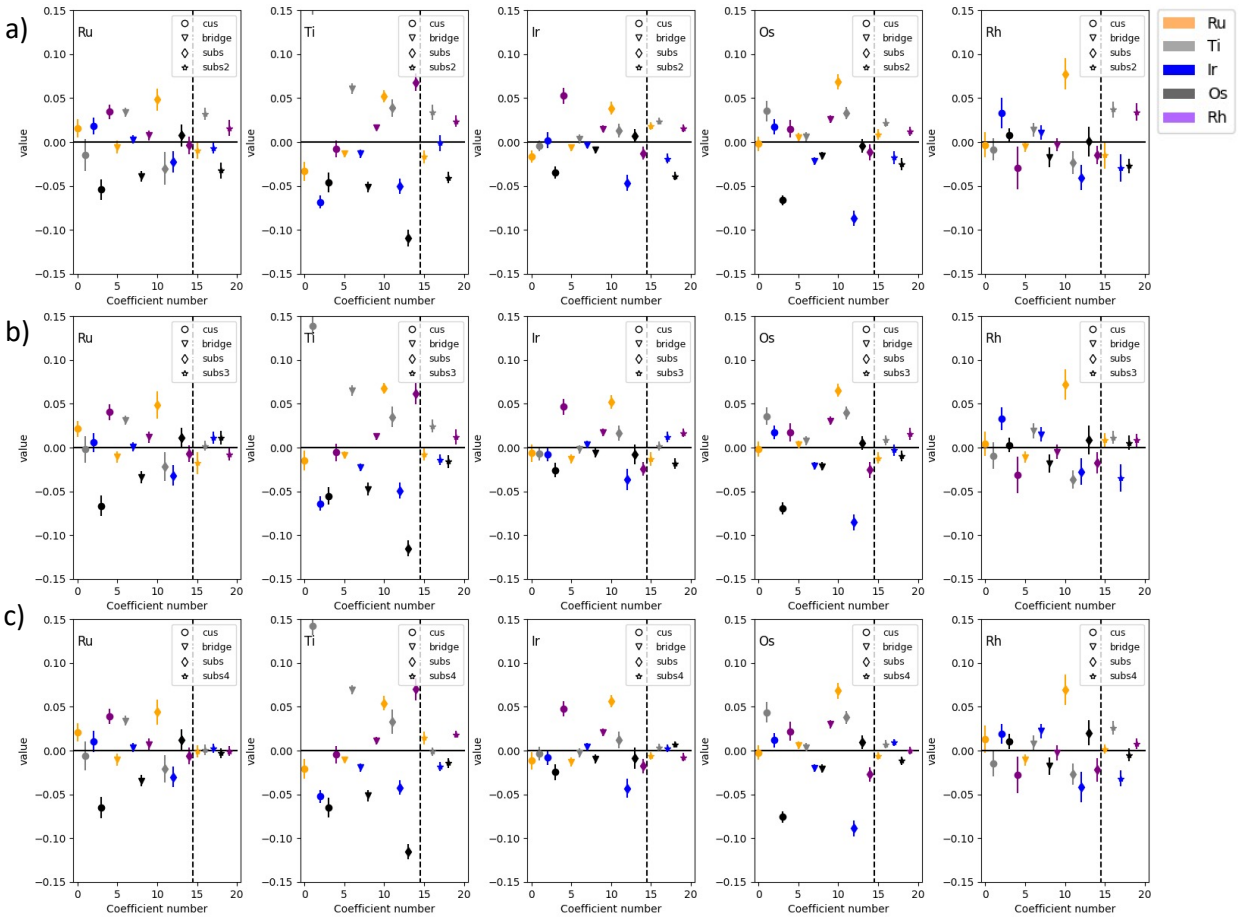

FIG. S10. Fitting coefficients for the adsorption of OH when including atoms marked a) sub2, b) sub3 and c) sub4 in the subsurface layer. The five plots refer to each of the five metals as adsorption sites as written in the top corner. The colour of each marker indicate the identity of the atom in the NN position. Markers to the right of the dashed line are the new coefficients included in the fit.

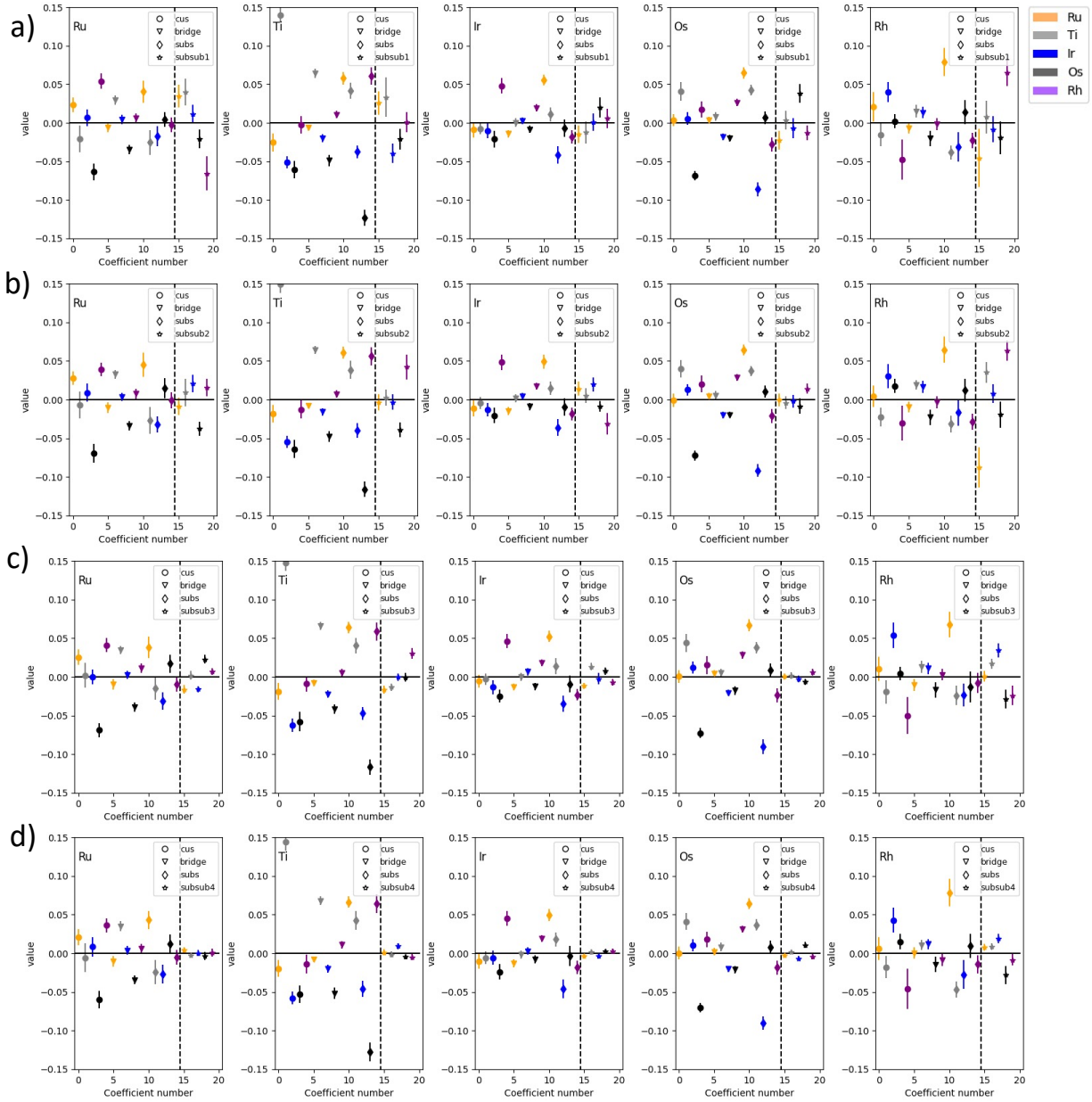

FIG. S11. Fitting coefficients for the adsorption of OH when including atoms marked a) subsub1, b) subsub2, c) subsub3 and d) subsub4 in the sub-subsurface layer. The five plots refer to each of the five metals as adsorption sites as written in the top corner. The colour of each marker indicate the identity of the atom in the NN position. Markers to the right of the dashed line are the new coefficients included in the fit.

S6. BRUTE-FORCE MODEL OF THE SURFACE

In the brute-force model a 100x100 surface is randomly generated for all possible compositions in 10% intervals. The fingerprints are generated for each cus and bridge site, and used to calculate the adsorption energy of *O and *OH/*O+H_b, while the *OOH/*O_2+H_b energies are calculated from the scaling relations for cus and bridge sites, respectively. For each bridge site it is decided if it will lower the energy if one of the two neighbouring cus sites transfer a proton from the *OH and/or *OOH intermediate. If a bridge site has two neighbouring cus sites that would both lower their energy by transfering a proton, it is assumed that only one of the two sites can do it. There are two different ways to decide which one; i) assuming that the proton is transferred to the bridge site from *OH/*OOH on the cus site, i.e. the cus site with the lowest *OH/*OOH energy can use the bridge site or ii) assuming that the *O+ H_b/*O_2 + H_b intermediate is formed directly, i.e. the cus site with the lowest *O/*O_2 energy can use the bridge. Each cus site likewise has two neighbouring bridge sites, and if both are free and result in a lower energy, the one with the lowest energy is chosen. Both approaches have been implemented but the results presented in the main paper are those of model (i). These are slightly different to the results of model (ii), but the most favourable composition remains a combination of Ru, Ir and possibly a small amount of Rh. Based on these results a refined search in 5% intervals is performed for all combinations of Ir, Ru and Rh. The optimum composition from the initial and the refined search at different potentials are given for the two different approaches in Table S3 and a plot equivalent to Figure 5 in the paper is inserted for model (ii) in Figure S12.

TABLE S3. Optimum composition at different potentials for the two different approaches described in the text after the initial (10%) scan and the refined (5%) scan for Ru,Ir and Rh combinations.

U/V	Opt. Comp. (i) Initial	Opt. Comp. (ii) initial	Opt. Comp. (i) refined	Opt. Comp. (ii) refined
1.45	$Ru_{0.4}Ir_{0.6}$	$Ru_{0.40}Ir_{0.40}Rh_{0.20}$	$Ru_{0.45}Ir_{0.55}$	$Ru_{0.35}Ir_{0.40}Rh_{0.25}$
1.55	$Ru_{0.5}Ir_{0.5}$	$Ru_{0.30}Ir_{0.50}Rh_{0.20}$	$Ru_{0.4}Ir_{0.55}Rh_{0.05}$	$Ru_{0.35}Ir_{0.40}Rh_{0.25}$
1.65	$Ru_{0.3}Ir_{0.7}$	$Ru_{0.30}Ir_{0.60}Rh_{0.10}$	$Ru_{0.35}Ir_{0.6}Rh_{0.05}$	$Ru_{0.35}Ir_{0.60}Rh_{0.05}$
1.75	$Ru_{0.3}Ir_{0.7}$	$Ru_{0.3}Ir_{0.7}$	$Ru_{0.3}Ir_{0.7}$	$Ru_{0.3}Ir_{0.7}$
1.85	$Ir_{1.0}$	$Ir_{1.0}$	$Ir_{1.0}$	$Ir_{1.0}$

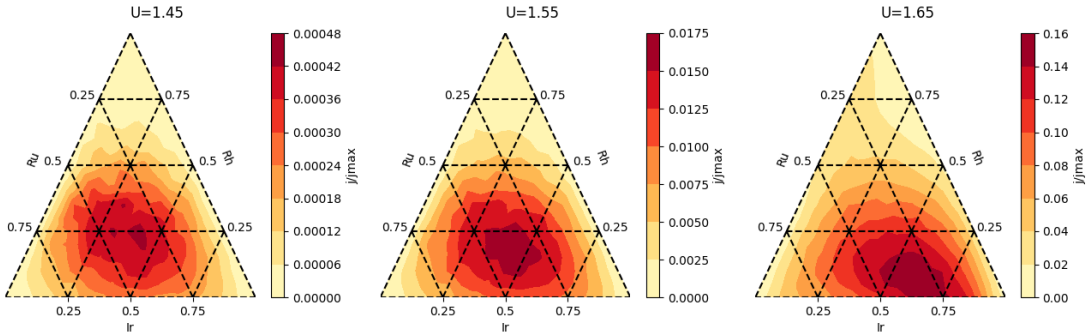

FIG. S12. Current as a function of composition obtained with model (ii) for combinations of Ru, Ir and Rh at a potential of a) 1.45 V, b) 1.55 V and c) 1.65 V.

To check that the basic model is correctly implemented, it is tested including the conventional pathway only, since the optimum composition can be found by direct optimisation using sequential least squares programming for this case. Note that several different starting guesses must be employed for the direct optimisation to ensure that the correct minimum is found; we use the equimolar composition as well as all bimetallic 50-50 combinations as starting guesses and take the result with the largest current from all of these optimisations. The optimum compositions are compared in Table S4, demonstrating that our model and the direct optimisation produce similar results after the refined search.

TABLE S4. Optimum composition at different potentials found using our brute-force model and by direct optimisation after the initial (10%) scan and the refined (5%) scan.

U/V	Opt. Comp. Our model, initial	Opt. Comp. Our model, refined	Opt. Comp. Direct opt.
1.55	$Ti_{0.3}Rh_{0.7}$	$Ti_{0.25}Os_{0.05}Rh_{0.7}$	$Ti_{0.29}Os_{0.04}Rh_{0.67}$
1.65	$Ti_{0.3}Rh_{0.7}$	$Ti_{0.3}Rh_{0.7}$	$Ti_{0.29}Os_{0.04}Rh_{0.67}$
1.75	$Ru_{0.3}Ti_{0.6}Os_{0.1}$	$Ti_{0.55}Os_{0.45}$	$Ti_{0.60}Os_{0.40}$

A. Choice of diffusion current

Figure S13 shows the diffusion current for different values of j_d on a common scale and relative to the maximum current $j_{max} = j_d N$ where N is the number of sites on the surface. Clearly, in the latter plot the curves are simply shifted along the x-axis.

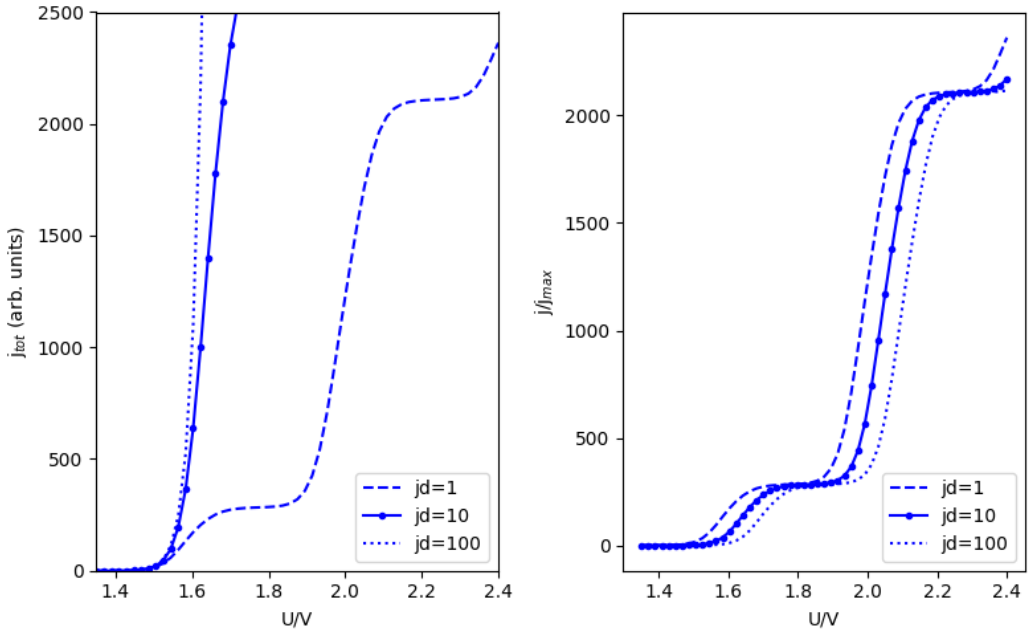

FIG. S13. Current vs potential for $Ru_{0.9}Ir_{0.1}O_2$ with model (i) for different choices of jd a) on a common scale and b) relative to the maximum possible current.

REFERENCES

[1]J. J. Mortensen, L. B. Hansen and K. W. Jacobsen, *Phys. Rev. B*, 2005, **71**, 035109.

[2]J. Enkovaara, C. Rostgaard, J. J. Mortensen, J. Chen, M. Dułak, L. Ferrighi, J. Gavnholt, C. Glinsvad, V. Haikola, H. A. Hansen, H. H. Kristoffersen, M. Kuisma, A. H. Larsen, L. Lehtovaara, M. Ljungberg, O. Lopez-Acevedo, P. G. Moses, J. Ojanen, T. Olsen, V. Petzold, N. A. Romero, J. Stausholm-Møller, M. Strange, G. A. Tritsaris, M. Vanin, M. Walter, B. Hammer, H. Häkkinen, G. K. H. Madsen, R. M. Nieminen, J. K. Nørskov, M. Puska, T. T. Rantala, J. Schiøtz, K. S. Thygesen and K. W. Jacobsen, *Journal of Physics: Condensed Matter*, 2010, **22**, 253202.

[3]A. H. Larsen, J. J. Mortensen, J. Blomqvist, I. E. Castelli, R. Christensen, M. Dułak, J. Friis, M. N. Groves, B. Hammer, C. Hargus, E. D. Hermes, P. C. Jennings, P. B. Jensen, J. Kermode, J. R. Kitchin, E. L. Kolsbjerg, J. Kubal, K. Kaasbjerg, S. Lysgaard, J. B. Maronsson, T. Maxson, T. Olsen, L. Pastewka, A. Peterson, C. Rostgaard, J. Schiøtz, O. Schütt, M. Strange, K. S. Thygesen, T. Vegge, L. Vilhelmsen, M. Walter, Z. Zeng and K. W. Jacobsen, *Journal of Physics: Condensed Matter*, 2017, **29**, 273002.

[4]B. Hammer, L. B. Hansen and J. K. Nørskov, *Phys. Rev. B*, 1999, **59**, 7413–7421.

[5]D. B. Rogers, R. D. Shannon, A. W. Sleight and J. L. Gillson, *Inorg. Chem.*, 1969, **8**, 841.

[6]J. K. Nørskov, J. Rossmeisl, A. Logadottir, L. Lindqvist, J. R. Kitchin, T. Bligaard and H. Jónsson, *The Journal of Physical Chemistry B*, 2004, **108**, 17886–17892.

[7]J. Rossmeisl, A. Logadottir and J. Nørskov, *Chemical Physics*, 2005, **319**, 178 – 184.

[8]I. E. L. Stephens, A. S. Bondarenko, U. Grønbjerg, J. Rossmeisl and I. Chorkendorff, *Energy Environ. Sci.*, 2012, **5**, 6744–6762.

[9]D.-Y. Kuo, J. K. Kawasaki, J. N. Nelson, J. Kloppenburg, G. Hautier, K. M. Shen, D. G. Schlom and J. Suntivich, *Journal of the American Chemical Society*, 2017, **139**, 3473–3479.

[10]D.-Y. Kuo, H. Paik, J. Kloppenburg, B. Faeth, K. M. Shen, D. G. Schlom, G. Hautier and J. Suntivich, *Journal of the American Chemical Society*, 2018, **140**, 17597–17605.

[11]K. A. Stoerzinger, L. Qiao, M. D. Biegalski and Y. Shao-Horn, *The Journal of Physical Chemistry Letters*, 2014, **5**, 1636–1641.

[12]L. G. V. Briquet, M. Sarwar, J. Mugo, G. Jones and F. Calle-Vallejo, *ChemCatChem*, 2017, **9**, 1261–1268.

[13]S. Divanis, A. M. Frandsen, T. Kutlusoy and J. Rossmeisl, *Phys. Chem. Chem. Phys.*, 2021, **23**, 19141–19145.

[14]J. Wellendorff, K. T. Lundgaard, A. Møgelhøj, V. Petzold, D. D. Landis, J. K. Nørskov, T. Bligaard and K. W. Jacobsen, *Phys. Rev. B*, 2012, **85**, 235149.

[15]C. Schelp, *An Alternative Way to Plot the Covariance Ellipse*, `https://carstenschelp.github.io/2018/09/14/Plot_Confidence_Ellipse_001.html`, 2018.

[16]I. C. Man, H.-Y. Su, F. Calle-Vallejo, H. A. Hansen, J. I. Martínez, N. G. Inoglu, J. Kitchin, T. F. Jaramillo, J. K. Nørskov and J. Rossmeisl, *ChemCatChem*, 2011, **3**, 1159–1165.